

Physics Contribution

MRI-based Assessment of 3D Intrafractional Motion of Head and Neck Cancer for Radiation Therapy



Oliver J. Gurney-Champion, PhD,^{*} Dualta McQuaid, PhD,^{*}
Alex Dunlop, PhD,^{*} Kee H. Wong, MD,[†] Liam C. Welsh, MD, PhD,[†]
Angela M. Riddell, MD,[‡] Dow-Mu Koh, MD,[‡] Uwe Oelfke, PhD,^{*}
Martin O. Leach, PhD,[§] Christopher M. Nutting, MD, PhD,^{||}
Shreerang A. Bhide, MD,^{||} Kevin J. Harrington, MD, PhD,^{*}
Rafal Panek, PhD,[¶] and Kate L. Newbold, MD[†]

^{}Joint Department of Physics, The Institute of Cancer Research and The Royal Marsden NHS Foundation Trust, London, UK; [†]Departments of [†]Clinical Oncology, [‡]Radiology, The Royal Marsden NHS Foundation Trust, London, UK; [§]CR UK Cancer Imaging Centre, The Institute of Cancer Research and The Royal Marsden NHS Foundation Trust, London, UK; ^{||}Joint Department of Radiotherapy, The Institute of Cancer Research and The Royal Marsden NHS Foundation Trust, London, UK; and [¶]Department of Medical Physics and Clinical Engineering, Nottingham University Hospitals NHS Trust, Nottingham, UK*

Received Jul 25, 2017, and in revised form Sep 14, 2017. Accepted for publication Oct 3, 2017.

Summary

This study assessed the 3-dimensional intrafractional motion of tumors from rapid 3-dimensional magnetic resonance imaging data of 56 patients with head and neck

Purpose: To determine the 3-dimensional (3D) intrafractional motion of head and neck squamous cell carcinoma (HNSCC).

Methods and Materials: Dynamic contrast-enhanced magnetic resonance images from 56 patients with HNSCC in the treatment position were analyzed. Dynamic contrast-enhanced magnetic resonance imaging consisted of 3D images acquired every 2.9 seconds for 4 minutes 50 seconds. Intrafractional tumor motion was studied in the 3 minutes 43 seconds of images obtained after initial contrast enhancement. To assess tumor

Reprint requests to: Oliver J. Gurney-Champion, PhD, Joint Department of Physics, The Institute of Cancer Research and The Royal Marsden NHS Foundation Trust, 15 Cotswold Rd, Sutton, London SM2 5NG, United Kingdom. Tel: 0044(0)2086613490; E-mail: oliver.gurney-champion@icr.ac.uk

O.J.G.-C. was responsible for the statistical analysis.

This work was supported by the Cancer Research UK Programme (grants C46/A10588, C7224/A13407, C7224/A23275, and C33589/A19727), Cancer Research UK Centres Network Accelerator Award (grant A21993) to the Cancer Research UK Advanced Radiotherapy Technologies Network (ART-NET) consortium, and Cancer Imaging Centre (grant C1060/A16464), as well as the National Institute for Health Research

Royal Marsden and The Institute of Cancer Research Biomedical Research Centre and Clinical Research Facility.

Conflict of interest: M.O.L. is a National Institute for Health Research Emeritus Senior Investigator. K.J.H. is a National Institute for Health Research Senior Investigator.

Supplementary material for this article can be found at www.redjournal.org.

Acknowledgments—We thank Wyke Huizinga from Erasmus University Medical Center Rotterdam for helping optimize the principal component analysis based group-wise rigid 3-dimensional transformation in Elastix used in this study. We also thank Dr Dominik Nickel from Siemens Healthineers for providing the non-product measurement sequence used in this research.

squamous cell carcinoma. The data showed that drifts due to systematic motion were <1.4 mm, drifts due to random motion were <2.1 mm, intrafractional tumor motion was larger for tumors in the hypopharynx and larynx than for tumors in the oropharynx, and the bony anatomy was a poor surrogate for tumor motion.

motion, rigid registration (translations only) was performed using a region of interest (ROI) mask around the tumor. The results were compared with bulk body motion from registration to all voxels. Motion was split into systematic motion and random motion. Correlations between the tumor site and random motion were tested. The within-subject coefficient of variation was determined from 8 patients with repeated baseline measures. Random motion was also assessed at the end of the first week (38 patients) and second week (25 patients) of radiation therapy to investigate trends of motion.

Results: Tumors showed irregular occasional rapid motion (eg, swallowing or coughing), periodic intermediate motion (respiration), and slower systematic drifts throughout treatment. For 95% of the patients, displacements due to systematic and random motion were <1.4 mm and <2.1 mm, respectively, 95% of the time. The motion without an ROI mask was significantly ($P < .0001$, Wilcoxon signed rank test) less than the motion with an ROI mask, indicating that tumors can move independently from the bony anatomy. Tumor motion was significantly ($P = .005$, Mann-Whitney U test) larger in the hypopharynx and larynx than in the oropharynx. The within-subject coefficient of variation for random motion was 0.33. The average random tumor motion did not increase notably during the first 2 weeks of treatment.

Conclusions: The 3D intrafractional tumor motion of HNSCC is small, with systematic motion <1.4 mm and random motion <2.1 mm 95% of the time. © 2017 The Authors. Published by Elsevier Inc. This is an open access article under the CC BY-NC-ND license (<http://creativecommons.org/licenses/by-nc-nd/4.0/>).

Introduction

Radiation therapy (RT) for head and neck squamous cell carcinoma (HNSCC) aims to deliver high radiation doses to the target volume while sparing the organs at risk. The availability of in-room cone beam computed tomography (CBCT) has enabled more accurate patient setup and minimized interfractional uncertainties (1-3). Furthermore, advances in intensity modulated RT (4, 5), such as volumetric modulated arc therapy (6, 7), enable more conformal dose distributions that better spare the organs at risk. However, such gains are limited by patient misalignment due to tumor motion between the CBCT and treatment delivery and during treatment.

To limit intrafractional tumor motion in HNSCC and to improve patient positioning reproducibility, patients are treated in a thermoplastic shell (8-10). However, motion may still be possible when the shell does not adequately immobilize patients, for instance, when patients lose weight during treatment. Furthermore, internal motion caused by swallowing (11, 12), respiration, or muscle tension and relaxation can occur.

Tumor motion has previously been estimated using radiographic imaging techniques such as portal imaging (13, 14) and computed tomography (15). However, several drawbacks are related to radiographic imaging for motion tracking. Because x-rays are ionizing radiation, imaging has been used sparingly, resulting in poor temporal resolution (at most 1 image every 3 minutes). Furthermore, soft tissue is often poorly depicted on radiographic images, and the bony anatomy is tracked instead. Whether HNSCC tumor motion is reflected in the motion of the bony anatomy remains to be investigated.

In contrast to radiographic imaging, magnetic resonance imaging (MRI) does not use ionizing radiation. Furthermore,

MRI offers high soft tissue contrast, enabling excellent definition of tumors (16, 17) including HNSCC (18). Tumor motion as a result of swallowing has previously been studied using fast 2-dimensional (2D) MRI acquisitions (11, 12). However, such techniques only assess motion in 2 directions, and through-plane motion can yield misleading measurements.

A promising alternative MRI dataset to study tumor motion is dynamic contrast-enhanced (DCE) MRI. DCE MRI uses the contrast enhancement of tumors over time (typically >4 minutes) to assess several tissue perfusion parameters. To study these properties, DCE MRI requires both high temporal resolution and high spatial resolution. Therefore, DCE acquisition protocols always aim to have the best trade-off between spatial and temporal resolution. Modern protocols allow for rapid (ie, approximately every 3 seconds) 3-dimensional (3D) imaging (19, 20). Furthermore, DCE MRI often uses T1-weighted sequences to study contrast enhancement, which are considered one of the best image types for depicting head and neck tumors (21). The aim of this study was to determine the 3D intrafractional motion of HNSCC.

Methods and Materials

Patients and treatment

This retrospective study was based on MRI scans of patients with HNSCC obtained as part of the INSIGHT study (22). Patients were recruited at The Royal Marsden Hospital between July 2013 and August 2016. The institutional review board (CCR3926) and research ethics committee

(13/LO/0067) approved this study (NCRI H&N CSG ID 13860). All patients gave written informed consent. Of the 56 patients analyzed, 36 received only chemoradiation therapy (CRT) and 20 received induction chemotherapy (IC) prior to CRT. Both treatment regimens were in accordance with local institution protocols. Treatment details and patient characteristics are provided in [Appendix E1](#) (available online at www.redjournal.org).

Imaging

Patients underwent multiple MRI examinations. The IC-CRT patients underwent MRI examinations prior to the first cycle of IC, prior to the second cycle of IC (3 weeks into treatment), prior to CRT (6 weeks into treatment), and 1 week into CRT (7 weeks into treatment). The CRT-only patients underwent MRI examinations prior to CRT, 1 week into CRT, and 2 weeks into CRT. For 8 patients, the MRI examination prior to treatment was repeated on separate days to assess test-retest precision.

All images were acquired on 1.5-T scanners (Magnetom Aera; Siemens Healthineers, Erlangen, Germany) across 2 hospital sites. To replicate the RT treatment position, patients were set up on a flat-top MRI couch using a shoulder board, headrest, and 5-point thermoplastic shell. A large flex and spine coil array was used as described earlier (22).

All MRI examinations consisted of multiple image acquisitions, including T1-weighted, T2-weighted, diffusion-weighted, and DCE images. Only the DCE images were analyzed in this study. The DCE acquisition was a series of 100 repeated 3D volume acquisitions (dynamic image) with a 2.9-second temporal resolution and a total acquisition time of 4 minutes 50 seconds. Each repeated measure was acquired using a 3D spoiled dual gradient echo with a $200 \times 200 \times 88\text{-mm}^3$ axial field of view; $2 \times 2 \times 2\text{-mm}^3$ voxels; repetition time of 7.2 ms, first echo time of 2.4 ms, and second echo time of 4.8 ms; flip angle of 24° ; bandwidth of 450 Hz/pixel; and the non-product measurement sequence options time-resolved angiography with interleaved stochastic trajectories (TWIST) view sharing, (A/B=33/33%) and controlled aliasing in parallel imaging results in higher acceleration (CAIPIRINHA) parallel imaging (acceleration factor R=4) for acceleration (23). Dotarem (Guerbet, Villepinte, France; 0.2 mg/kg, 2 mL/s, followed by a 20-mL saline solution flush) was administered during the 10th dynamic acquisition as a bolus through a peripherally placed cannula using an automatic injector.

Analyses

A radiation oncologist (K.H.W.), in consensus with a consultant radiologist (A.M.R.), used RayStation (version 4.6.1; RaySearch Laboratories, Stockholm, Sweden) to delineate the primary tumor volumes (region of interest [ROI]) under guidance of the T1-weighted, T2-weighted, and diffusion-weighted images. In 10 patients the primary

tumor was absent after diagnostic tonsillectomy, so a spherical target volume (2 cm^3) was placed within the target bed (KLN). Further image processing was performed in MATLAB (version 2016b; The MathWorks, Natick, MA), making use of the image registration program Elastix (version 4.8) (24, 25). All statistical analyses were done in the R program (version 3.3.2 [2016]; R Foundation for Statistical Computing, Vienna, Austria) (26).

The ROIs were transferred to the subsequent MRI examinations. Per the DCE image dataset (all dynamic images from 1 examination), a mean DCE image was generated. The mean DCE image from the first MRI examination was registered to the mean DCE images from the subsequent MRI examinations using the Euler transformation in Elastix. The transformation parameters were applied to the ROI to create ROIs for all DCE image datasets.

For each DCE image dataset, we registered the dynamic images to each other using rigid 3D transformation in Elastix, making use of the group-wise principal component analysis-based dissimilarity metric described by Huizinga et al (27). This metric was found to outperform other common metrics typically used for registration of functional images, including DCE images (27). Additional registration options used were as follows: reduced-dimension B-spline interpolator (order 1 during iterations, order 3 for final image); adaptive stochastic gradient descent optimizer; PCAMetric2; and an initial registration at half resolution, followed by a final registration at full resolution. The ROI was dilated by 8 mm (4 voxels) to create an ROI mask containing the tumor and some adjacent reference tissue. Only voxels within this ROI mask were considered in the registration's cost function. Elastix returned right-left (RL), anterior-posterior (AP), and foot-head (FH) transformations for each dynamic image that best overlaid the tumor on the different dynamic images, such that the registration represented the inverted tumor motion. We inverted the transformation to obtain the tumor position for each dynamic image (hence, as a function of time). From here onward, $dx(t)$, $dy(t)$, and $dz(t)$ indicate the tumor position for RL, AP, and FH, respectively, as a function of time (t). Positive numbers indicate the left, anterior, and head directions.

To minimize the effect of contrast injection (during acquisition of the 10th dynamic image) and contrast inflow (approximately the first 40 seconds after injection), the first 1 minute 7 seconds of tumor positions was discarded. This resulted in 223 seconds (3 minutes 43 seconds) of motion data per DCE image dataset, which is similar to typical volumetric modulated arc therapy times (28).

Baseline motion

We determined the effects of typical systematic and random intrafractional tumor motion on tumor position. For systematic motion, the mean [dx , dy , dz] from each of the dynamic images (3 minutes 43 seconds) was subtracted from the mean [dx , dy , dz] during the last 4 dynamic images. The last 4 dynamic images were used as a reference

as they were least affected by contrast inflow. For random motion, the location of the tumor ($[dx(t), dy(t), dz(t)]$) with respect to the average location of the tumor (mean $[dx, dy, dz]$) was determined for each dynamic image. Probability density function plots of tumor position due to systematic and random motion were plotted. We defined the maximum systematic shift as the 95th percentile of the 3D offset ($\sqrt{dx^2 + dy^2 + dz^2}$) due to systematic motion. We defined the maximum random 3D shift per patient as the 95th percentile of all random shifts ($MAX_{95,pp}$). The overall maximum random shift (MAX_{95}) was defined as the 95th percentile over all patients' $MAX_{95,pp}$. The 95th percentiles were used because maxima are sensitive to outliers. The vector magnitude of standard deviations of $[dx(t), dy(t), dz(t)]$ was used as patient-specific motion magnitude (SD_{3D}).

To assess the bulk motion of the head and neck within the thermoplastic shell, the analyses were repeated without an ROI mask during image registration (considering all voxels in the cost function). A Wilcoxon signed rank test (significance level $\alpha=.05$) between SD_{3D} values from registrations with and without an ROI mask tested whether tumor motion was different from bulk motion. All further analyses were performed on the results from the image registrations with an ROI mask.

Typically, a 0.5- to 1-minute CBCT acquisition is used to determine patient positioning immediately prior to RT delivery. To assess the motion between the CBCT acquisition and treatment, we plotted the difference from the mean $[dx, dy, dz]$ from the first quarter (55 seconds) of dynamic images to the mean $[dx, dy, dz]$ during the second, third, and fourth quarters.

The patient-specific SD_{3D} was plotted per tumor site to assess tumor site-specific motion. A 2-sided Mann-Whitney U test ($\alpha=.05$) between the SD_{3D} of oropharyngeal tumors versus hypopharyngeal and laryngeal tumors was used to test for differences in motion magnitude among anatomic sites.

Repeated measures

To evaluate the test-retest precision of the SD_{3D} , we calculated the within-subject coefficient of variation (wCV) for the repeated pretreatment DCE image datasets. A Bland-Altman plot was plotted for these data.

Motion throughout sessions

For 38 patients (25 CRT-only and 13 IC-CRT patients), DCE MRI was acquired during all MRI examinations throughout treatment. For these patients, we plotted the SD_{3D} for the different treatment stages. To assess typical SD_{3D} changes throughout treatment, we calculated the wCV of the SD_{3D} during treatment. To test whether the effect of treatment on the SD_{3D} was larger than day-to-day variations, we performed a Mann-Whitney U test ($\alpha=.05$)

between values of SD^2M^2 of the SD_{3D} from the repeated baseline measures and throughout treatment, where SD^2M^2 was the SD over the repeated measures of SD_{3D} divided by the squared population mean of SD_{3D} .

Results

Figure 1 shows an example of a typical DCE MRI image set from this study. Figure 2 shows examples of tumor motion associated with swallowing, respiration, or drifting of the tumor. Figure E1 (available online at www.redjournal.org) shows 3D motion tracks for a representative group of patients.

Baseline motion

Both systematic motion and random motion were most pronounced in the FH direction and least pronounced in the RL direction (Fig. 3a-d). For 95% of all patients, motion caused systematic tumor shifts of <1.4 mm (0.4 mm, 0.6 mm, and 1.1 mm for RL, AP, and FH, respectively) and random tumor shifts of <2.1 mm (MAX_{95} ; 0.9 mm, 1.6 mm, and 2.0 mm for RL, AP, and FH, respectively)—that is, the tumor was within 2.1 mm of the mean position 95% of the time (Fig. 4).

The motion of the head and neck within the thermoplastic shell (Fig. 3e-h) was significantly ($P<.0001$) less than the motion of the tumor (Fig. 3a-d). This finding indicates that tumor motion was independent of the immobilized head and neck.

The distance between the tumor during the initial 55 seconds and the tumor during subsequent 55-second periods increased over time, from 0.4 ± 0.3 mm (second quarter; mean \pm standard deviation over patients) to 0.5 ± 0.4 mm (third quarter) to 0.7 ± 0.5 mm (fourth quarter) (Fig. 5). The tumor position during the fourth 55-second period was, on average, 0.7 ± 0.5 mm (mean \pm standard deviation over patients; 0.3 ± 0.2 mm, 0.4 ± 0.3 mm, and 0.6 ± 0.4 mm for RL, AP, and FH, respectively) away from its initial position, with a maximum shift up to 2.6 mm (0.8 mm, 1.7 mm, and 2.4 mm for RL, AP, and FH, respectively). The motion trail of the patient showing the maximum displacement (brown line in Fig. 5) is shown in Figure 2d and Figure E2 (available online at www.redjournal.org).

Hypopharyngeal and laryngeal tumors had a significantly ($U=286$, $P=.005$) higher motion magnitude (median SD_{3D} , 0.9 mm; quartiles, 0.8-1.1 mm) than oropharyngeal tumors (median SD_{3D} , 0.4 mm; quartiles, 0.3-0.7 mm) (Fig. 6).

Repeated measures

The wCV for the SD_{3D} was 0.34 for the repeated baseline acquisitions (Fig. E4; available online at www.redjournal.org).

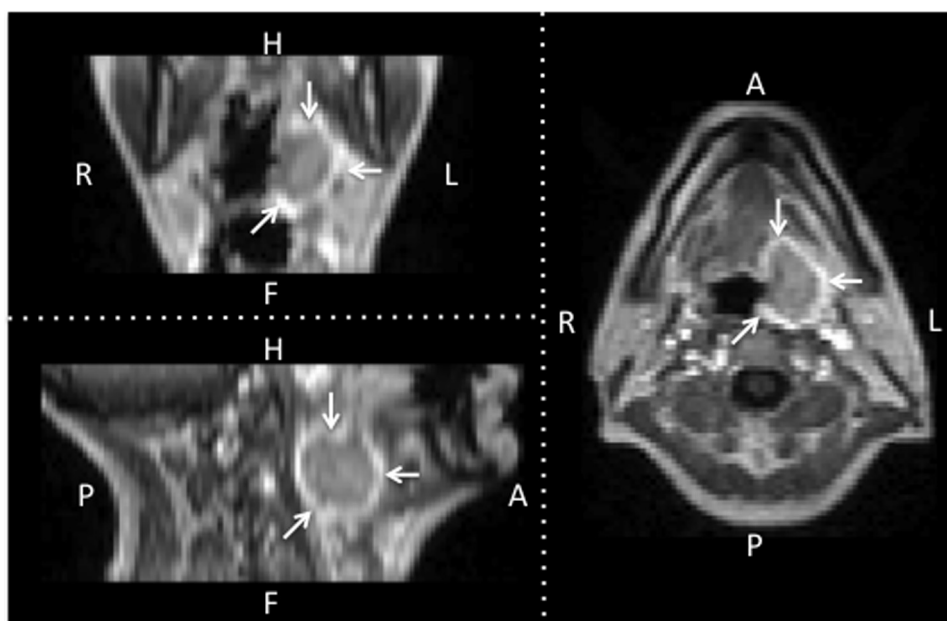


Fig. 1. Different cross sections (coronal [top left], sagittal [bottom left], and transverse [right]) of the 50th dynamic image (116 seconds after contrast injection) from a dynamic contrast-enhanced dataset. The arrows depict the patient's untreated oropharynx head and neck squamous cell carcinoma. A = anterior; F = foot; H = head; L = left; P = posterior; R = right.

Motion throughout sessions

The wCV for the repeated SD_{3D} through treatment was 0.41 for CRT-only patients and 0.45 for IC-CRT patients. These wCVs were not significantly different from the wCV of the repeated measures ($P=.70$ for CRT-only patients and $P=.80$ for IC-CRT patients), and no global trends were observed during the first 2 weeks of treatment (Fig. E5; available online at www.redjournal.org).

Discussion

We analyzed 3D intrafractional tumor motion for HNSCC patients using 3 minutes 43 seconds of DCE MRI data obtained in the treatment position. Tumors show irregular occasional rapid motion (eg, swallowing), periodic motion (respiration), and slower systematic drifts throughout treatment. The 95th percentiles of the systematic and random motion components contributed to maximum displacements of 1.4 mm and 2.1 mm, respectively. We demonstrated that tumors can move independently from the head and neck, confirming that the bony anatomy is a poor surrogate for tumor motion. Intrafractional tumor motion was significantly larger for tumors in the hypopharynx and larynx than for tumors in the oropharynx. On average, intrafractional tumor motion did not increase notably during the first 2 weeks of treatment.

Linear accelerators (LINACs) often require a minute-long CBCT scan for patient positioning. Figure 5 shows that when patient positioning is completed with longer

acquisitions (55 seconds) and treatment is simulated as a 55-second period 0 seconds, 55 seconds, and 1 minute 50 seconds after position verification, the systematic mismatch between treatment and position verification on average is 0.4 ± 0.3 mm, 0.5 ± 0.4 mm, and 0.7 ± 0.5 mm (mean \pm standard deviation), respectively. It should be noted that these systematic tumor motion definitions reflect trends in tumor motion during a treatment fraction. The systematic error might average out over sessions and be combined with the random component.

The 95th percentile over patients of the 95th percentile of all random shifts ($MAX_{95,pp}$) was 2.1 mm. However, 1 patient showed a much higher $MAX_{95,pp}$ of 4.6 mm (Fig. 4). This large tumor motion was a result of both respiration and swallowing (Fig. E3; available online at www.redjournal.org).

When image registration is not guided by an ROI mask, the motion is smaller than when guided by an ROI mask (Fig. 3). These findings suggest that HNSCC moves independently of the remaining anatomy. We assume that bulk motion of the head and neck is representative of bulk motion of the bony anatomy. In that case, motion of the bony anatomy is not a perfect surrogate for tumor motion. This agrees with findings from other tumor sites (29). Therefore, studies based on radiographic imaging may underestimate the tumor motion, and systems tracking the bony anatomy during treatment (30, 31) are of limited value for patients with HNSCC.

Tumors in inferior regions (hypopharynx and larynx) showed significantly more intrafractional motion than oropharyngeal tumors. Tumor subsites in the lower neck are more prone to swallowing- and respiration-related motions.

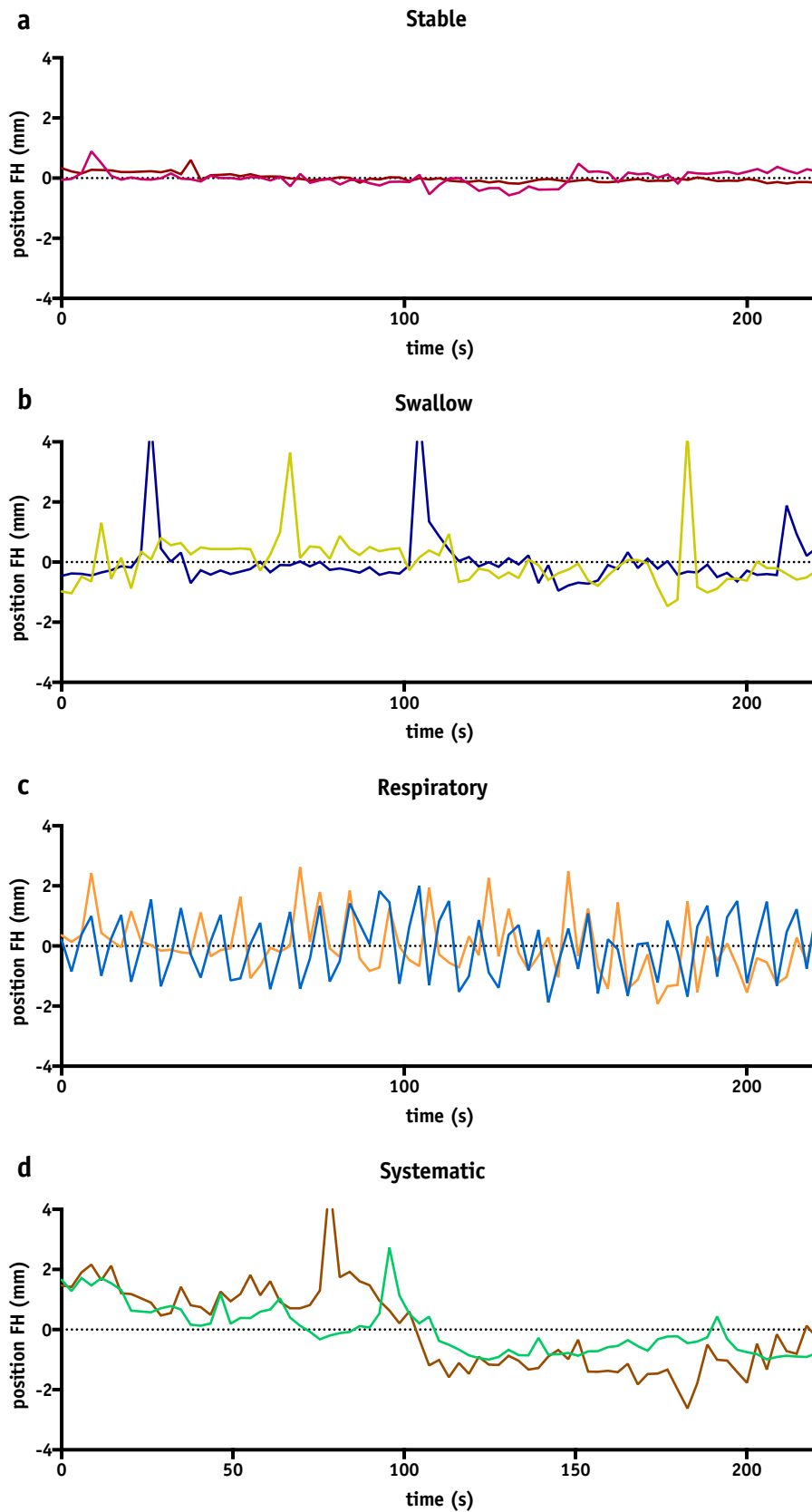


Fig. 2. Motion in foot-head (FH) directions from selected patients (color coded) as a function of time. The graphs include a selection of tumors that were relatively stable (a), moved during swallowing (b), moved with respiration (c), or showed a drift (d).

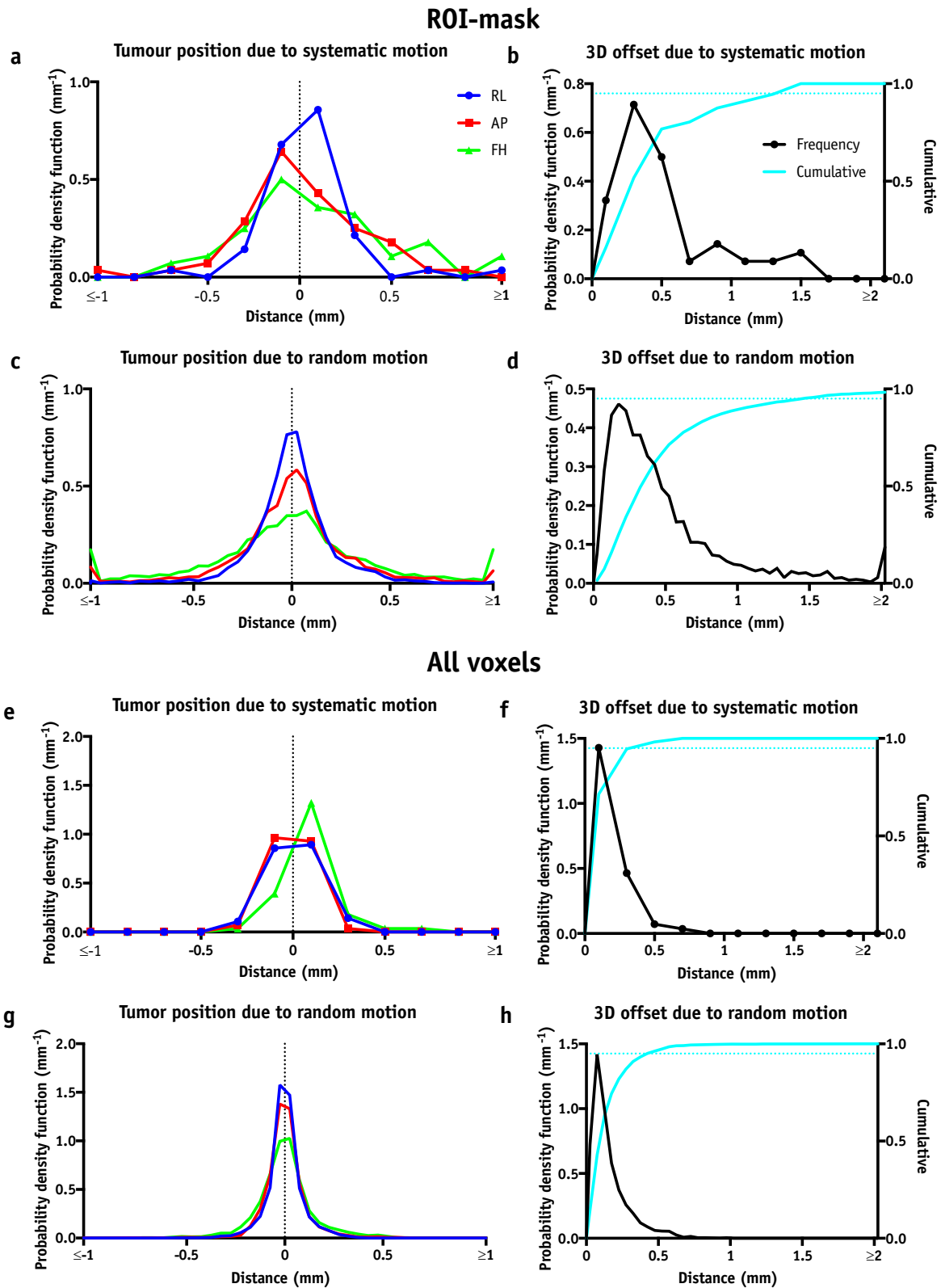


Fig. 3. Probability density functions of tumor positions due to motion (systematic [a, b, e, f] and random [c, d, g, h]) of head and neck squamous cell carcinoma for 3 individual directions (a, c, e, g) and 3-dimensionally (3D) (b, d, f, h). The cumulative probability (solid blue lines) and 95% cumulative probability (dotted blue lines) are shown in b, d, f, and h. Results with (a-d) and without (e-h) a region of interest (ROI) mask are shown. AP = anterior-posterior; FH = foot-head; RL = right-left. (A color version of this figure is available at www.redjournal.org.)

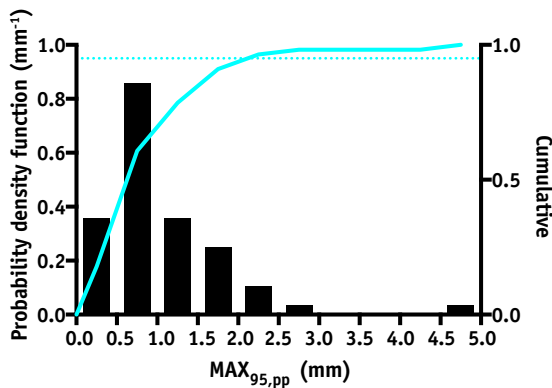


Fig. 4. Probability density functions (histogram) and cumulative probability (solid line) of 95th percentile of all random shifts per patient ($MAX_{95,pp}$). The motion track of the outlier with $MAX_{95,pp}$ of 4.6 mm is shown in [Figure E3](#).

These observations could potentially be used to guide individualized planning target volumes for different tumor subsites during RT planning.

Intrafractional motion magnitude was characterized as the SD_{3D} . The SD_{3D} had a test-retest precision (wCV) of 0.33, suggesting a 95% confidence interval that a patient's SD_{3D} should not change $>91\%$ from day to day $\sqrt{2} \times 1.96 \times 0.33 \times 100\%$ [32]. The wCV of the SD_{3D} from the repeated DCE MRI through the first 2 weeks of treatment was not significantly different from the SD_{3D} before treatment. Furthermore, there was no substantial change in mean SD_{3D} throughout treatment ([Fig. E5](#); available online at [www.redjournal.org](#)). Therefore, we conclude that there is no large effect of treatment on the SD_{3D} during the first 2 weeks of RT.

To deal with setup uncertainties, such as from tumor motion, target volumes are expanded by a safety margin. For patients with HNSCC, the margins are often on the order of 3 to 5 mm (7, 13, 14, 33). The observed motion is within these margins.

Our imaging might underestimate motion from timescales comparable to the acquisition time (2.9 seconds). Two studies used rapid (0.15-second) 2D MRI to assess tumor motion and found that swallowing occurs 0 to 1.5 times per minute, lasts 3.5 seconds on average, and causes shifts of 4.0 to 11.6 mm (11, 12). For such irregular and infrequent motion, the tumor is only briefly at a potentially missed location during RT, and the dosimetric effect is limited.

However, the dosimetric effects of repetitively missing the tumor due to respiratory motion may be larger. Our sequence did pick up periodic motion that could be associated with respiration ([Fig. 2c](#)); however, the acquisition frequency of 0.34 Hz (2.9 seconds per image) is close to the Nyquist frequency for determining the frequency of typical respiration (0.17 Hz, 6 seconds per image). This is reflected in the fact that there are approximately 10 peaks every 100 seconds in [Figure 2c](#) (blue line), whereas typical patient breathing frequencies are higher. As the acquisition speed of the protocol (2.9 seconds) is shorter than the typical respiratory cycle and

as MRI image composition is determined at the center of k-space, which is acquired much more quickly, MRI will sample representative tumor positions from the respiratory cycle each acquisition. This results in correctly estimating the magnitude of motion as long as the respiratory motion is monitored long enough to obtain a large enough representative sample of tumor positions. This is illustrated in [Appendix E5](#) (available online at [www.redjournal.org](#)), in which we used the Quasar MRI-Compatible Respiratory Motion Phantom (Modus Medical Devices, London, Ontario, Canada). In the limited set of patients who show respiratory motion of the tumor, it might be preferable to include the respiratory motion in the treatment plan using faster 2D imaging protocols (11, 12, 34) or 4-dimensional MRI (35, 36) or to track motion during treatment using a magnetic resonance-guided RT system (37).

Several studies have attempted to determine intrafractional motion using radiographic imaging (13, 14, 38-42). These studies often only obtained 2 images per treatment session and only monitored motion of the bony anatomy. Therefore, comparing results is challenging, and we limit ourselves to the most comparable study, performed by Suzuki et al (13). They acquired 6 projection images in 3-minute intervals. Their systematic intrafractional motion (0.2-0.8 mm) and random intrafractional motion (0.3-0.6 mm) were similar to our findings without an ROI mask and lower than our findings for tumor motion ([Fig. 3](#)). This substantiates our assumption that image registration without an ROI mask was representative of motion of the bony anatomy. The 2 studies depicting tumor motion on MRI found a mean maximum resting shift (excluding swallowing motion) of 1.5 to 3.1 mm (11, 12), which is larger than our systematic displacement of 1.4 mm. This is possibly explained by the longer time over which they quantified the shifts, 12 minutes 48 seconds, as compared with our observation time (3 minutes 43 seconds).

In this research DCE images were used to study tumor motion. These images have several advantages over alternative sequences, the main advantage being that the contrast enhancement improved the signal-to-noise ratio and tumor conspicuity. Without the contrast-enhanced signal-to-noise ratio and tumor contrast, monitoring tumor position at such high spatial and temporal resolution would be challenging using similar acquisition protocols. Furthermore, DCE imaging protocols are often optimized for speed and resolution, as DCE modeling requires both. When motion is being assessed without contrast enhancement, alternative sequences might be more useful, such as balanced steady-state free precession (bSSFP) (36, 37, 43) or alternating repetition time bSSFP (44, 45), which have a more T2-like contrast.

Most of the observed motion was at the sub-voxel (<2 mm) level. However, image registration algorithms are not limited by resolution and can pick up such motion accurately (46, 47). This is reflected in [Figure 2a](#), in which the spread in tumor positions is well below voxel level. Furthermore, [Figure E8](#) (available online at [www.redjournal.org](#)) shows that motion

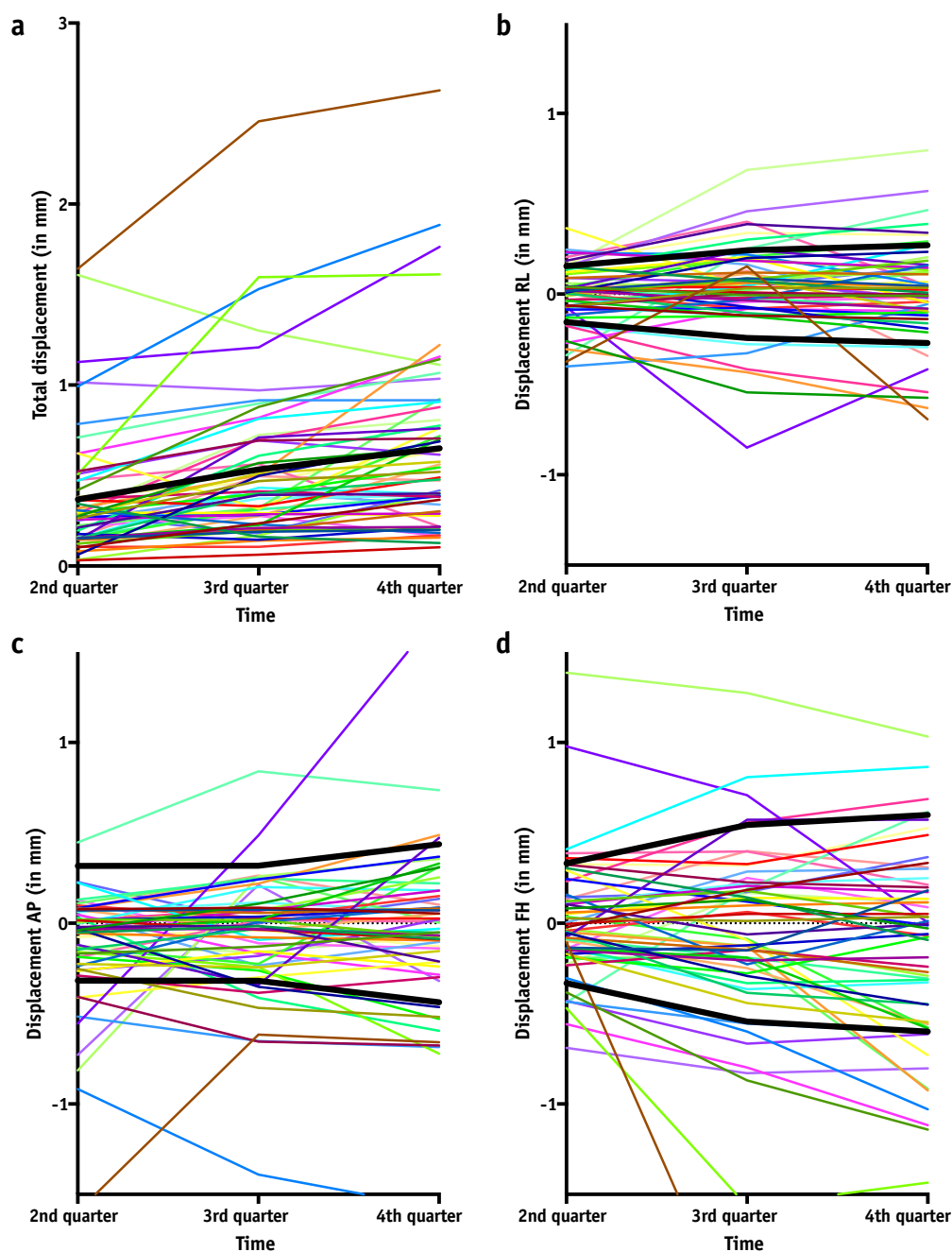


Fig. 5. Mean position of tumor averaged over 55-second intervals compared with mean position at initial 55-second interval. The colors indicate the individual tumor positions for each patient, and the black line indicates the mean position (a) or mean \pm standard deviation of positions (b-d). The color scheme is identical to that used in Figure 2. AP = anterior-posterior; FH = foot-head; RL = right-left. (A color version of this figure is available at www.redjournal.org.)

of 0.2 mm of the Quasar Motion Phantom is detectable using our sequence.

Contrast enhancement of the tumor and surrounding tissue occurred during the acquisition. On one hand, the contrast enhancement could have influenced the registration. Therefore, we discarded data from the first 40 seconds after contrast injection, during which image contrast changed most, and used an image registration algorithm that was not based on contrast being similar over time. To

test whether contrast enhancement had influenced the results, we compared the results from registration from patients showing large drifts (>1 mm for AP, RL, or FH) with manually determined motion by placing landmarks on images (Appendix E5, Figs. E6 and E7; available online at www.redjournal.org). This comparison shows that the registrations were not influenced by contrast inflow. On the other hand, the improved signal-to-noise ratio and tumor conspicuity improved image registration.

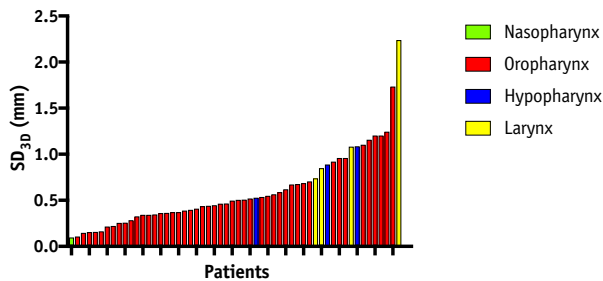


Fig. 6. Standard deviation of tumor positions (SD_{3D}), sorted by their magnitude, colored per tumor site.

Rotations and deformations were ignored during registration. This simplified the interpretation. Furthermore, the effect of rotations on the dose to the primary tumor is often limited (48, 49). Visual inspection of videos from the DCE images after registration showed stable tumor position after registration, supporting the performance of the methodology. We repeated the analysis with the Euler transformation and found similar results (results not shown).

The patients in this study were examined with MRI outside the treatment room and not an MRI-LINAC system or ordinary LINAC system. However, care was taken to have setup as close as possible to typical treatment setup, using a flat-top MRI couch, shoulder board, headrest, 5-point thermoplastic shell, and coil holders to make sure the coil did not deform the patient contour. This would especially reflect a treatment setup on an MRI-LINAC system, as the LINAC is positioned behind the MRI bore in such a system. Therefore, we believe that the motion monitored is representative of motion during treatment, in particular on an MRI-LINAC system.

Conclusions

Head and neck tumors can show irregular occasional rapid motion (eg, swallowing), periodic motion (respiration), and slower systematic drifts throughout treatment. Systematic motion was <1.4 mm, and random motion was <2.1 mm. Reassuringly, these are well within clinical safety margins. The bony anatomy is a poor surrogate for tumor motion as tumor motion is significantly larger than bulk head and neck motion. Intrafractional tumor motion is significantly larger for tumors in the hypopharynx and larynx than for tumors in the oropharynx. Average intrafractional tumor motion does not increase significantly during the first 2 weeks of RT.

References

- Guckenberger M, Meyer J, Vordermark D, et al. Magnitude and clinical relevance of translational and rotational patient setup errors: A cone-beam CT study. *Int J Radiat Oncol Biol Phys* 2006;65:934-942.
- Jaffray DA, Siewerdsen JH, Wong JW, et al. Flat-panel cone-beam computed tomography for image-guided radiation therapy. *Int J Radiat Oncol Biol Phys* 2002;53:1337-1349.
- Den RB, Doemer A, Kubicek G, et al. Daily image guidance with cone-beam computed tomography for head-and-neck cancer intensity-

- modulated radiotherapy: A prospective study. *Int J Radiat Oncol* 2010;76:1353-1359.
- Eisbruch A, Ship JA, Dawson LA, et al. Salivary gland sparing and improved target irradiation by conformal and intensity modulated irradiation of head and neck cancer. *World J Surg* 2003;27:832-837.
- Braam PM, Terhaard CHJ, Roesink JM, et al. Intensity-modulated radiotherapy significantly reduces xerostomia compared with conventional radiotherapy. *Int J Radiat Oncol Biol Phys* 2006;66:975-980.
- Otto K. Volumetric modulated arc therapy: IMRT in a single gantry arc. *Med Phys* 2008;35:310-317.
- Verbakel WF, Cuijpers JP, Hoffmans D, et al. Volumetric intensity-modulated arc therapy vs. conventional IMRT in head-and-neck cancer: A comparative planning and dosimetric study. *Int J Radiat Oncol Biol Phys* 2009;74:252-259.
- Niewald M, Lehmann W, Uhlmann U, et al. A customized head and neck support system. *Radiother Oncol* 1988;11:55-63.
- Bentel GC, Marks LB, Hendren K, et al. Comparison of two head and neck immobilization systems. *Int J Radiat Oncol Biol Phys* 1997;38:867-873.
- Gilbeau L, Octave-Prignon M, Loncol T, et al. Comparison of setup accuracy of three different thermoplastic masks for the treatment of brain and head and neck tumors. *Radiother Oncol* 2001;58:155-162.
- Bradley JA, Paulson ES, Ahunbay E, et al. Dynamic MRI analysis of tumor and organ motion during rest and deglutition and margin assessment for radiotherapy of head-and-neck cancer. *Int J Radiat Oncol Biol Phys* 2011;81:803-812.
- Paulson ES, Bradley JA, Wang D, et al. Internal margin assessment using cine MRI analysis of deglutition in head and neck cancer radiotherapy. *Med Phys* 2011;38:1740-1747.
- Suzuki M, Nishimura Y, Nakamatsu K, et al. Analysis of interfractional set-up errors and intrafractional organ motions during IMRT for head and neck tumors to define an appropriate planning target volume (PTV)- and planning organs at risk volume (PRV)-margins. *Radiother Oncol* 2006;78:283-290.
- Pang PP, Hendry J, Cheah SL, et al. An assessment of the magnitude of intra-fraction movement of head-and-neck IMRT cases and its implication on the action-level of the imaging protocol. *Radiother Oncol* 2014;112:437-441.
- Drabik DM, MacKenzie MA, Fallone GB. Quantifying appropriate PTV setup margins: Analysis of patient setup fidelity and intrafraction motion using post-treatment megavoltage computed tomography scans. *Int J Radiat Oncol Biol Phys* 2007;68:1222-1228.
- Gurney-Champion OJ, Versteijne E, van der Horst A, et al. Addition of MRI for CT-based pancreatic tumor delineation: A feasibility study. *Acta Oncol (Madr)* 2017;56:923-930.
- Rasch CR, Steenbakkers RJ, Fitton I, et al. Decreased 3D observer variation with matched CT-MRI, for target delineation in nasopharynx cancer. *Radiat Oncol* 2010;5:21.
- Rasch C, Keus R, Pameijer FA, et al. The potential impact of CT-MRI matching on tumor volume delineation in advanced head and neck cancer. *Int J Radiat Oncol Biol Phys* 1997;39:841-848.
- Gaddikeri S, Gaddikeri RS, Taylor T, et al. Dynamic contrast-enhanced MR imaging in head and neck cancer: Techniques and clinical applications. *AJNR Am J Neuroradiol* 2016;37:588-595.
- Panek R, Schmidt MA, Borri M, et al. Time-resolved angiography with stochastic trajectories for dynamic contrast-enhanced MRI in head and neck cancer: Are pharmacokinetic parameters affected? *Med Phys* 2016;43:6024-6032.
- Wippold FJ. Head and neck imaging: The role of CT and MRI. *J Magn Reson Imaging* 2007;25:453-465.
- Welsh L, Panek R, McQuaid D, et al. Prospective, longitudinal, multimodal functional imaging for radical chemo-IMRT treatment of locally advanced head and neck cancer: The INSIGHT study. *Radiat Oncol* 2015;10:112.
- Michaely HJ, Morelli JN, Budjan J, et al. CAIPIRINHA-Dixon-TWIST (CDT)-volume-interpolated breath-hold examination (VIBE): A new

- technique for fast time-resolved dynamic 3-dimensional imaging of the abdomen with high spatial resolution. *Invest Radiol* 2013;48:590-597.
24. Klein S, Staring M, Murphy K, et al. Elastix: A toolbox for intensity-based medical image registration. *IEEE Trans Med Imaging* 2010;29:196-205.
 25. Shamonin D. Fast parallel image registration on CPU and GPU for diagnostic classification of Alzheimer's disease. *Front Neuroinform* 2013;7:1-15.
 26. R Core Team. R: A Language and Environment for Statistical Computing. Vienna, Austria: R Foundation for Statistical Computing; 2016.
 27. Huizinga W, Poot DH, Guyader JM, et al. PCA-based groupwise image registration for quantitative MRI. *Med Image Anal* 2016;29:65-78.
 28. Bertelsen A, Hansen CR, Johansen J, et al. Single arc volumetric modulated arc therapy of head and neck cancer. *Radiother Oncol* 2010;95:142-148.
 29. van der Horst A, Wognum S, Dávila Fajardo R, et al. Interfractional position variation of pancreatic tumors quantified using intratumoral fiducial markers and daily cone beam computed tomography. *Int J Radiat Oncol Biol Phys* 2013;87:202-208.
 30. Gurney-Champion OJ, Dahele M, Mostafavi H, et al. Digital tomosynthesis for verifying spine position during radiotherapy: A phantom study. *Phys Med Biol* 2013;58:5717-5733.
 31. Verbakel WFAR, Gurney-Champion OJ, Slotman BJ, et al. Sub-millimeter spine position monitoring for stereotactic body radiotherapy using offline digital tomosynthesis. *Radiother Oncol* 2015;115:223-228.
 32. Bland JM, Altman DG. Statistical methods for assessing agreement between two methods of clinical measurement. *Lancet* 1986;1:307-310.
 33. van Kranen S, van Beek S, Rasch C, et al. Setup uncertainties of anatomical sub-regions in head-and-neck cancer patients after offline CBCT guidance. *Int J Radiat Oncol Biol Phys* 2009;73:1566-1573.
 34. Lens E, Gurney-Champion O, Tekelenburg D, et al. Abdominal organ motion during inhalation and exhalation breath-holds: Pancreatic motion at different lung volumes compared. *Radiother Oncol* 2016;121:268-275.
 35. Freedman JN, Collins DJ, Bainbridge H, et al. T2-weighted 4D magnetic resonance imaging for application in magnetic resonance-guided radiotherapy treatment planning. *Invest Radiol* 2017;52:563-573.
 36. Stemkens B, Tijssen RH, De Senneville BD, et al. Optimizing 4-dimensional magnetic resonance imaging data sampling for respiratory motion analysis of pancreatic tumors. *Int J Radiat Oncol Biol Phys* 2015;91:571-578.
 37. Li H, Chen HC, Dolly S, et al. An integrated model-driven method for in-treatment upper airway motion tracking using cine MRI in head and neck radiation therapy. *Med Phys* 2016;43:4700-4710.
 38. Cacicedo J, Perez JF, Ortiz de Zarate R, et al. A prospective analysis of inter- and intrafractional errors to calculate CTV to PTV margins in head and neck patients. *Clin Transl Oncol* 2014;17:113-120.
 39. Ohtakara K, Hayashi S, Tanaka H, et al. Clinical comparison of positional accuracy and stability between dedicated versus conventional masks for immobilization in cranial stereotactic radiotherapy using 6-degree-of-freedom image guidance system-integrated platform. *Radiother Oncol* 2012;102:198-205.
 40. Linthout N, Verellen D, Tournel K, et al. Six dimensional analysis with daily stereoscopic x-ray imaging of intrafraction patient motion in head and neck treatments using five points fixation masks. *Med Phys* 2006;33:504-513.
 41. Kim S, Akpati HC, Kielbasa JE, et al. Evaluation of intrafraction patient movement for CNS and head & neck IMRT. *Med Phys* 2004;31:500-506.
 42. Verbakel WF, Lagerwaard FJ, Verduin AJ, et al. The accuracy of frameless stereotactic intracranial radiosurgery. *Radiother Oncol* 2010;97:390-394.
 43. Oppelt A, Graumann R, Barfuss H, et al. FISP—A new fast MRI sequence. *Electromedica* 1986;54:15-18.
 44. Gurney-Champion OJ, Nederveen AJ, Klaassen R, et al. Revisiting the potential of alternating repetition time balanced steady-state free precession imaging of the abdomen at 3 T. *Invest Radiol* 2016;51:560-568.
 45. Leupold J, Hennig J, Scheffler K. Alternating repetition time balanced steady state free precession. *Magn Reson Med* 2006;55:557-565.
 46. Hajnal JV, Saeed N, Oatridge A, et al. Detection of subtle brain changes using subvoxel registration and subtraction of serial MR images. *J Comput Assist Tomogr* 1995;19:677-691.
 47. Puri BK, Hutton SB, Saeed N, et al. A serial longitudinal quantitative MRI study of cerebral changes in first-episode schizophrenia using image segmentation and subvoxel registration. *Psychiatry Res* 2001;106:141-150.
 48. Fu W, Yang Y, Yue NJ, et al. Dosimetric influences of rotational setup errors on head and neck carcinoma intensity-modulated radiation therapy treatments. *Med Dosim* 2013;38:125-132.
 49. Kim GY, Pawlicki T, Le QT, et al. Linac-based on-board imaging feasibility and the dosimetric consequences of head roll in head-and-neck IMRT plans. *Med Dosim* 2008;33:93-99.